

Background Rejection in the DMTPC Dark Matter Search Using Charge Signals

J.P. Lopez^{a,b,*}, D. Dujmic^{a,b}, S. Ahlen^c, J.B.R. Battat^{a,d,1}, C. Deaconu^{a,b},
P. Fisher^{a,b,e,f}, S. Henderson^{a,b}, A. Inglis^c, A. Kaboth^{a,b}, J. Monroe^{a,h},
G. Sciolla^{a,g,1}, H. Tomita^c, H. Wellenstein^g, R. Yamamoto^a

^a*Physics Department, Massachusetts Institute of Technology; Cambridge, MA 02139, USA*

^b*Laboratory for Nuclear Science, Massachusetts Institute of Technology; Cambridge, MA 02139, USA*

^c*Physics Department, Boston University; Boston, MA 02215, USA*

^d*Physics Department, Bryn Mawr College; Bryn Mawr, PA 19010, USA*

^e*MIT Kavli Institute for Astrophysics and Space Research, Massachusetts Institute of Technology; Cambridge, MA 02139, USA*

^f*Institute for Soldier Nanotechnology, Massachusetts Institute of Technology; Cambridge, MA 02139, USA*

^g*Physics Department, Brandeis University; Waltham, MA 02453, USA*

^h*Physics Department, Royal Holloway, University of London; Egham, TW20 0EX, UK*

Abstract

The Dark Matter Time Projection Chamber (DMTPC) collaboration is developing a low pressure gas TPC for detecting Weakly Interacting Massive Particle (WIMP)-nucleon interactions. Optical readout with CCD cameras allows for the detection of the daily modulation of the direction of the dark matter wind. In order to reach sensitivities required for WIMP detection, the detector needs to minimize backgrounds from electron recoils. This paper demonstrates that a simplified CCD analysis achieves 7.3×10^{-5} rejection of electron recoils while a charge analysis yields an electron rejection factor of 3.3×10^{-4} for events with ^{241}Am -equivalent ionization energy loss between 40 keV and 200 keV. A combined charge and CCD analysis yields a background-limited upper limit of 1.1×10^{-5} (90% confidence level) for the rejection of γ and electron events. Backgrounds from alpha decays from the field cage are eliminated by introducing a veto electrode that surrounds the sensitive region in the TPC. CCD-specific backgrounds are reduced more than two orders of magnitude when requiring a coincidence with the charge readout.

Keywords: Dark matter, WIMP, TPC, CCD, Dark matter wind, Direct detection, Directional detection

1. Introduction

In recent years, dark matter direct detection experiments have obtained seemingly contradictory results, both supporting the existence of WIMP dark matter [1–3] and setting ever more stringent limits on its interaction cross section

*Corresponding Author
Preprint submitted to Elsevier
Email address: jplopez@mit.edu (J.P. Lopez)

¹Present Address

24 with nucleons [4, 5]. The tension between these experimental results highlights
25 the need for a detection strategy that provides an unambiguous measurement
26 capable of distinguishing between WIMP-nucleus scattering events and back-
27 ground nuclear recoils. The strong expected directional signature of WIMP-
28 induced recoils, due to the motion of the earth through the galactic dark matter
29 halo, may provide such an unambiguous evidence of WIMP-nucleus scatter-
30 ing [6, 7]. A number of experimental groups are developing detectors to search
31 for this signal [8], and techniques have been developed to analyze data with
32 directional information to extract the possible directional signal of WIMP dark
33 matter [9–14].

34 The DMTPC collaboration uses a low-pressure time projection chamber
35 (TPC) to search for WIMP-nucleon elastic scattering from WIMPs in the local
36 dark matter halo. The TPC is filled with CF_4 gas to take advantage of the
37 expected favorable WIMP- ^{19}F spin-dependent cross section [15]. The WIMP
38 interaction signature is a low-momentum nuclear recoil that leaves an ioniza-
39 tion trail in the detector. Primary-ionization electrons from nuclear recoils are
40 amplified [16] and the scintillation light from these avalanches is imaged by a
41 charged-coupled device (CCD) camera. Using the shape of the ionization trail,
42 DMTPC detectors are able to identify the direction of the nuclear recoil. The
43 analysis of CCD tracks is described in [17].

44 Electrons from β decays and processes such as Compton scattering from γ -
45 and x-rays are typically important backgrounds in dark matter direct detection
46 sources. These can be due to radioactive contaminants in the materials used to
47 construct the detector, radioactive components of the target material, and ra-
48 dioactive material in the laboratory environment. Such events are often rejected
49 by fiducialization of the active volume. In experiments measuring the energy
50 loss due to multiple processes, such as ionization, scintillation, and phonon ex-
51 citation, these can further be identified by the relative fraction of energy loss
52 due to each process [4, 5]. Other experiments attempt to create detectors that
53 are wholly insensitive to electron recoils [18, 19]. Many of these techniques are
54 inapplicable to current directional detector designs, which typically measure
55 only the ionization component of recoil energy loss. Directional detection ex-
56 periments can instead use the low density of ionization from electron recoils to
57 identify and reject these events [20, 21].

58 This work describes the charge readout systems of a prototype DMTPC
59 detector and the corresponding analysis used to evaluate recoil properties such
60 as position, energy, and geometry. It presents several studies taken with this
61 detector in a surface laboratory at MIT. Section 2.1 describes the charge readout
62 systems of this detector and Section 3 describes event reconstruction.

63 In DMTPC detectors, the CCD readout is used to reconstruct the ionization
64 density projected onto a two-dimensional readout plane. The stopping power
65 of electrons typically falls within the CCD read noise and is too low for these
66 events to be reconstructed, while the stopping power of α particles and nuclear
67 recoils is sufficient to accurately measure recoil properties. The charge signals,
68 which are sensitive to the total energy loss due to ionization, are able to measure
69 and identify electronic recoils. Section 4.1 describes a study using charge signals

70 to determine the ability of a DMTPC detector to reject electronic recoils and
71 to enhance the ability of the detector to reject these events through pulse shape
72 analysis.

73 For DMTPC detectors, a number of backgrounds from CCD readout artifacts
74 and interactions in the CCD bulk must also be eliminated in order to perform
75 a low-background WIMP search. Section 4.2 describes these backgrounds and
76 rejection strategies using the charge signals. It also discusses the use of a veto
77 region to identify and reject alpha decays from the outside the sensitive region.
78 In certain circumstances, α particles can be misinterpreted by the CCD as
79 nuclear recoils.

80 2. Detector Design

81 The data in this paper were taken with a detector in a surface lab in
82 Cambridge, Massachusetts using a 75 Torr CF_4 gas target. Figure 1 shows
83 a schematic of this detector. The field cage of the detector has a drift length of
84 10 cm with a wire mesh cathode held at -1.2 kV. The drift cage is constructed
85 of copper rings with a 27 cm inner diameter. The amplification region consists
86 of a stainless steel woven mesh separated by nonconductive spacers from an
87 anode plane made of copper-clad G10. The amplification mesh is coupled to an
88 amplifier with a 30Ω impedance to ground while the anode is biased at 680 V.
89 The separation is $440 \mu\text{m}$.

90 The scintillation light from electron amplification goes through a viewport
91 at the top of the vacuum vessel and into a Nikon f/1.2 lens with a focal length of
92 55 mm. The lens directs the light into an Apogee Alta U6 CCD camera, which
93 uses a Kodak KAF-1001 1024 x 1024 pixel CCD. The $24 \mu\text{m} \times 24 \mu\text{m}$ pixels are
94 binned on-chip into 4×4 blocks prior to digitization, resulting in a 256 bin x 256
95 bin image. The CCD images a $16.7 \text{ cm} \times 16.7 \text{ cm}$ square centered on the circular
96 anode. The remainder of the anode is not imaged. Each 4×4 pixel bin reads out
97 a $650 \mu\text{m} \times 650 \mu\text{m}$ region of the anode. An americium-241 α source was
98 used to determine a CCD energy calibration of 13.1 ± 0.1 analog-to-digital units
99 (ADU) per keV of energy loss contributing to ionization. The energy of the α
100 particles from the source is attenuated by a thin film, and the mean energy was
101 measured to be 4.44 MeV using an Ortec ULTRA ion-implanted-silicon detector
102 [22]. Calculations from SRIM [23] show that over 99% of the total energy loss of
103 α particles at these energies contributes to ionization at this energy. Measured
104 recoil energies in this paper are reported in α -equivalent energy units, denoted
105 keV_α . Because the energy loss is dominated by ionization, the α -equivalent
106 energy will be similar to the more standard electron-equivalent energy (in units
107 of keV_{ee}), which is difficult to determine in a detector that is largely insensitive
108 to electrons.

109 2.1. Charge Readout Systems

110 The anode plane has a diameter of 26.7 cm and is separated into two regions.
111 The outermost 1 cm, called the veto region, is used to identify ionization events

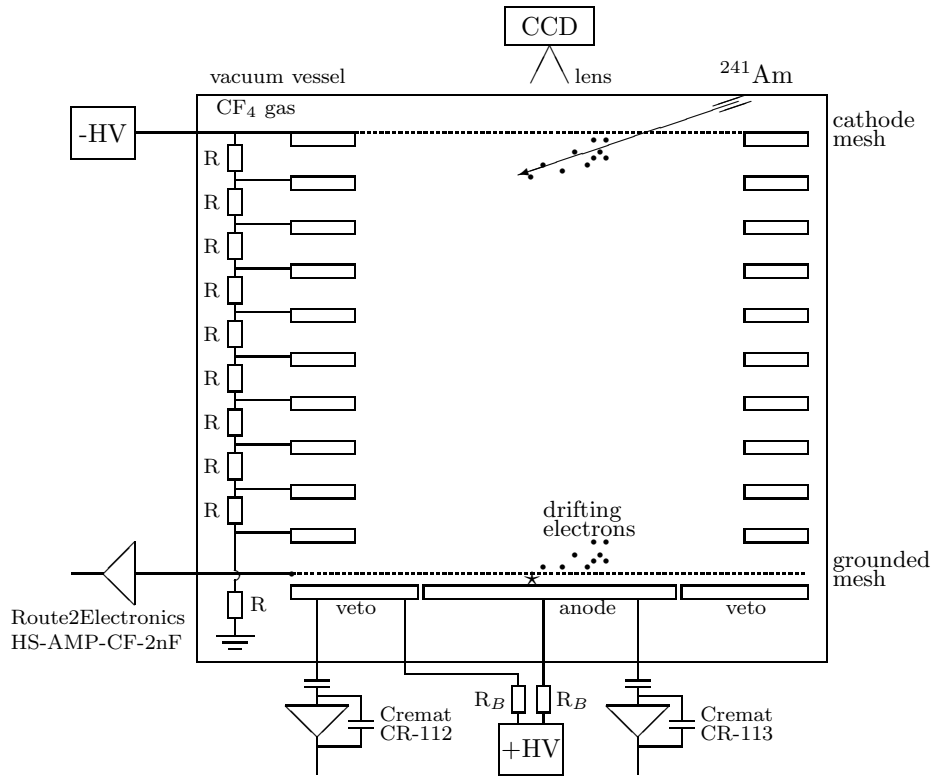
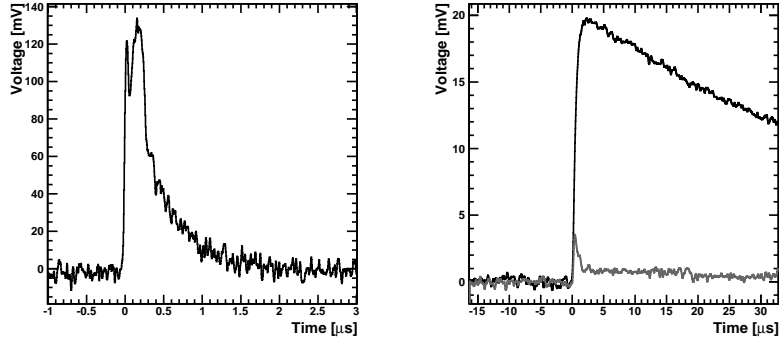


Figure 1: A schematic of the detector: the drift field is created by a cathode mesh, field-shaping rings attached to a resistor chain and a ground mesh. The drift cage has a height of 10 cm and a diameter of 27 cm. Primary ionization from a recoiling nucleus is drifted down to the ground mesh. The high-field amplification region is formed by the ground mesh and the anode plane. The grounded mesh is read out with a fast amplifier and the veto and anode are read out with charge-sensitive preamplifiers. The central anode region has a diameter of 24.7 cm. Scintillation light from the amplification region is recorded with the CCD camera.

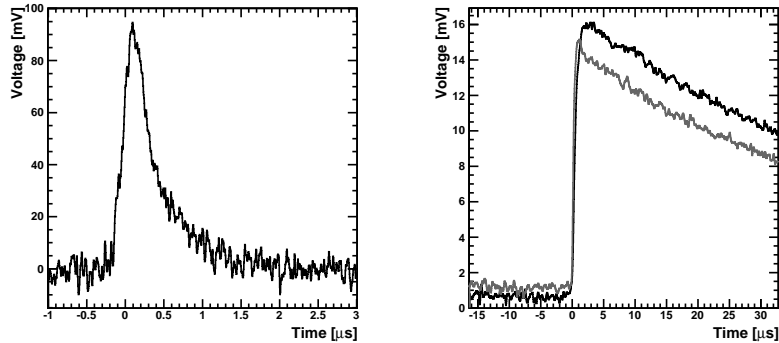
112 occurring near the field cage rings. The inner 24.7 cm diameter region, called
113 the anode region, is used to measure the energies of recoil events. Charge
114 signals from the anode region are amplified by a Cremat CR-113 charge sensitive
115 preamplifier (CSP) [24], while the signals from the veto region are amplified by
116 a Cremat CR-112 CSP. The gain of the CR-113 CSP is 1.5 mV/pC, and that
117 of the CR-112 CSP is 13 mV/pC. Both have a nominal rise time of 20 ns when
118 disconnected from the detector and a decay time of 50 μ s. Recoil events have
119 a typical rise time of approximately 1 μ s due to the ion drift velocity across
120 the amplification region, so the peak output voltage of the anode CSP gives a
121 very accurate measurement of the total track ionization. Low-energy α particles
122 from the ^{241}Am run described in Section 3.4, with $40 \text{ keV}_\alpha < E < 400 \text{ keV}_\alpha$,
123 give an energy calibration of 0.251 ± 0.003 mV per keV_α in the central anode
124 channel. There is a linear relationship between the energies measured in charge
125 and light in this energy range.

126 The amplification mesh is read out through a Route2Electronics HS-AMP-
127 CF preamplifier [25]. This preamplifier has a gain of 80 and a rise time of
128 roughly 1 ns when not connected to the detector. A 30 Ω resistor connects
129 the mesh and preamplifier input to ground so that the output is proportional
130 to the induced current from charged particles drifting in the amplification re-
131 gion. Most ionization in the amplification region happens very near the anode
132 so the electrons drift quickly over a very short distance while the ions drift more
133 slowly over a longer distance, from the anode toward the amplification mesh.
134 The induced current of the electrons from a single electron is a peak that decays
135 within several nanoseconds while the ions create a broader but smaller shoul-
136 der. Low-energy nuclear recoils create compact ionization trails, with a range
137 along the drift direction (Δz) of no more than a few millimeters. Because of
138 the electron drift velocity of approximately 10 cm/ μ s [26], all primary ioniza-
139 tion electrons reach the amplification region within a period of several tens of
140 nanoseconds. The electron signals of the avalanches add together to create a
141 fast rising edge and a sharp peak in the current signal. The ions drifting in
142 the amplification region then create a second, broader peak. This shape can be
143 seen in Fig. 2(a). In tracks with large Δz , such as most electronic recoils and
144 minimum ionizing particles, the spread in time of primary ionization electrons
145 entering the amplification region is long compared to the detector response of
146 an electron avalanche, and the resulting pulse is characterized by a single broad
147 peak from both the electrons and ions in the avalanche. Pulse shape analysis
148 in the charge channels (see Fig. 2) provides powerful discrimination between
149 nuclear and electronic recoils and can strongly suppress such backgrounds in a
150 rare-event search.

151 All charge signals are digitized by AlazarTech AT860 8-bit PCI digitizers
152 using a sampling rate of 250 MHz. The digitizer bandwidth extends up to 65
153 MHz. A total of 12288 samples (49.2 μ s) are saved with each trace, including
154 4096 pre-trigger samples (16.4 μ s). Charge events are triggered on the rising
155 edge of either the mesh channel signal at 75 mV or the central anode signal at
156 10 mV. This is sufficient to obtain a high expected efficiency for $E > 30 \text{ keV}_\alpha$.
157 During event readout the CCD is exposed for 1 s, while the digitizers collect



(a) Mesh (left), central anode (right, dark), and veto (right, light) signals from a 75 keV_α α track



(b) 60 keV_α e^- recoil, with signal from veto electrode

Figure 2: Example smoothed traces of (a) an α track and (b) a vetoed electronic recoil. Note the two-peaked structure of the mesh pulse in (a), which is absent in (b).

158 charge triggers. After each exposure the image and charge triggers (if any) are
 159 written to file for later processing and analysis. A camera shutter is not used so
 160 tracks occurring during the shifting and digitization of CCD pixels, a process
 161 taking approximately 200 ms, are seen in the CCD data but not in the charge
 162 data.

163 3. Event Reconstruction

164 3.1. CCD Tracks

165 Recoil candidates are selected using the energy, range and several geometric
 166 moments computed from the CCD image. In order to maximize the recoil
 167 analysis efficiency, less stringent cuts were used than those described in [17].

168 The CCD selection cuts are described in detail in Section 4.2. In Monte Carlo
169 studies, the CCD track finding and cuts achieve over 70% efficiency for ionization
170 yields greater than 40 keV $_{\alpha}$ and over 90% for ionization yields greater than
171 50 keV $_{\alpha}$.

172 *3.2. Anode and Veto Signals*

173 The anode and veto signals are first smoothed using a Gaussian convolution
174 with $\sigma = 80$ ns. The typical rise time of a pulse in these channels is 1 μ s, so
175 the smoothing reduces the noise while having little effect on the pulse shape.
176 The pre-trigger region is then used to determine the baseline voltage and noise
177 RMS. The pulse shape is characterized by its peak voltage and time and the
178 times on both the rising and falling edge where the pulse reaches 10%, 25%,
179 50%, 75% and 90% of the baseline-subtracted peak height.

180 *3.3. Mesh Signals*

181 For the mesh channel, a Gaussian convolution with $\sigma = 6$ ns is used to reduce
182 the noise. After smoothing, the 25% to 75% rise time of the initial sharp edge
183 of the electron signal in the data used in this paper is always greater than 15 ns.
184 The broadening due to the smoothing here is no more than approximately 10%.
185 Other features are less sensitive to the smoothing algorithm.

186 As with the anode and veto channels, the baseline voltage and noise RMS are
187 calculated from the pre-trigger samples. The initial electron peak of a nuclear
188 recoil candidate is identified as the first peak in a pulse with a height greater
189 than 50% of the total peak height. The ion peak is defined as the largest peak in
190 the pulse separated from the electron peak by more than 50 ns. The lowest point
191 between the two peaks is also measured. The pulse shape is also characterized
192 by similar rise and fall time variables as for the other channels. Rise times
193 are calculated between the initial pulse baseline crossing and the electron peak
194 and fall times between the ion peak and the baseline crossing at the end of the
195 pulse. If only a single peak is found, rise and fall times are calculated from that
196 peak. Single-peaked events occur rarely because the reconstruction algorithm
197 will typically identify a small noise fluctuation as an additional peak if no clear
198 second peak is present. Fig. 3 shows an annotated example of a mesh pulse
199 from an α particle.

200 *3.4. Nuclear Recoil Selection Criteria*

201 Selection criteria for nuclear recoils were determined by placing a ^{241}Am α
202 source above the cathode mesh and outside the active volume of the detector.
203 Most of the α energy is lost before crossing through the cathode into the active
204 volume, so that α tracks of tens to a few hundred keV in energy are measured.

205 Three sets of cuts are used to suppress background charge traces: (1) removal
206 of triggers on noise and other pathological events; (2) removal of signals from
207 tracks passing over the veto region; and (3) removal of events identified as
208 electronic recoils (Table 1).

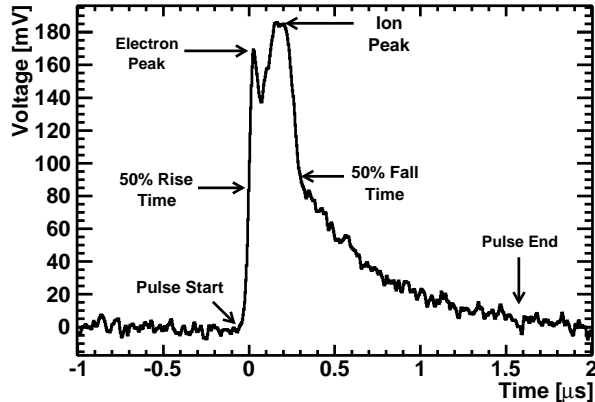


Figure 3: Annotated mesh pulse of a 115 keV $_{\alpha}$ α particle. A Gaussian convolution has been used to reduce the noise prior to pulse shape characterization. The pulse start and end points are the nearest baseline crossings to the peak. Rise times are calculated from the electron peak and fall times are calculated from the ion peak. For anode and veto pulses, only a single peak is identified.

Variable	Description
V_A	Peak anode channel voltage
V_V	Peak veto channel voltage
T_R^V	25% to 90% rise time of the veto channel
T_R^M	25% to 75% rise time of the mesh channel
V_e/V_A	Ratio of the mesh electron peak and the anode peak
V_i/V_A	Ratio of the mesh ion peak and the anode channel peak

Table 1: Description of reconstructed pulse shape variables used in analysis cuts.

209 The electronic noise-reduction cuts remove events with anomalous baseline
 210 voltages or noise RMS voltages. Any charge triggers due to noise on one of the
 211 channels are removed using cuts on the pulse rise and fall times. The analysis
 212 also checks that the full mesh pulse is included in the saved waveform and that
 213 the mesh and anode pulses are correlated in time. Charge events that saturate
 214 the digitizer for one of the charge channels are removed.

215 Events in the central anode region induce small pulses in the veto channel as
 216 well. Events actually passing through the veto region are rejected by requiring
 217 that $V_A > 4V_V$ and that $T_R^V < 400$ ns. Pulses with longer rise times show
 218 the characteristic shape of electron avalanches occurring in the amplification
 219 region above the veto channel and are rejected with the latter cut. Finally, a
 220 small population of pulses showing pileup effects are rejected by requiring time
 221 coincidence between the veto pulse and the mesh pulse. This population is very
 222 rare and typically only occurs when a radioactive source is placed inside the

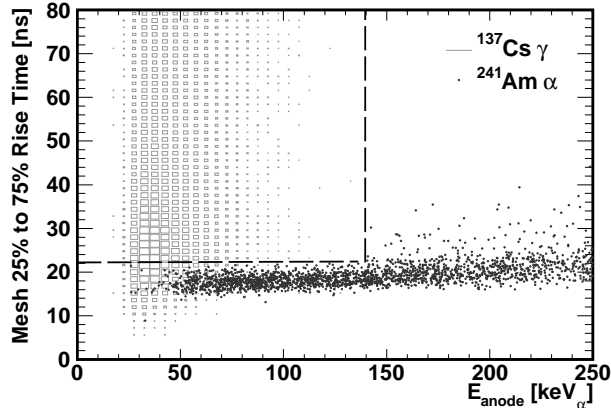


Figure 4: Mesh signal rise time of both electronic recoils and α tracks. The dashed line represents the selection cut used in this analysis to remove electrons.

223 detector.

224 Nuclear recoil candidates are then identified using the shape of the mesh
 225 pulse. The rise time is due to a combination of electron longitudinal diffusion
 226 during drift, electronics response and recoil Δz . Nuclear recoil candidates have
 227 $T_R^M < 22$ ns for ionization yields of less than 125 keV_α (Fig. 4). The compact
 228 tracks from nuclear recoils lead to generally larger but narrower peaks compared
 229 to electronic recoils of the same energy (Fig. 5). In this analysis, nuclear recoil
 230 candidates have $V_e/V_A > 4.5$ and $V_i/V_A > 5.5$.

231 Once a set of candidate nuclear recoil light signals (using the cuts described in
 232 Section 4.2) and a set of candidate nuclear recoil charge signals are identified, the
 233 event reconstruction attempts to match each track to its corresponding charge
 234 signal. To do this, all possible charge-light signal pairs are considered. The best
 235 match according to the relative charge-light energy calibration of $V_{\text{anode}}[mV] =$
 236 $(3.07 \pm 0.04) + (0.01916 \pm 0.00002)N_{\text{CCD}}[ADU]$ (Fig. 6), where V_{anode} is the
 237 peak height of the anode signal and N_{CCD} is the total number of ADU in the
 238 CCD track, is chosen. The match is accepted if the anode signal is less than 8.5
 239 mV (3.5σ) from the value estimated from the measured light signal.

240 At the energies measured here, the trail of ionization left by α particles is
 241 much longer than that left by fluorine and carbon recoils of the same energy. The
 242 α particles in the calibration data enter the field cage at a mean polar angle of
 243 approximately 45° and drift across the full length of the drift cage (see the source
 244 placement in Fig. 1), so the measured parts of the α tracks have more diffusion
 245 and Δz comparable to or longer than nuclear recoils oriented exactly along the
 246 drift (z)direction. Because of this, the cuts set using the ^{241}Am data will be
 247 valid for carbon and fluorine recoils as well. The efficiency of the charge cuts
 248 and charge-light energy matching for tracks identified in the CCD analysis was
 249 measured using the α data to be greater than 90% for $40 \text{ keV}_\alpha < E < 200 \text{ keV}_\alpha$.

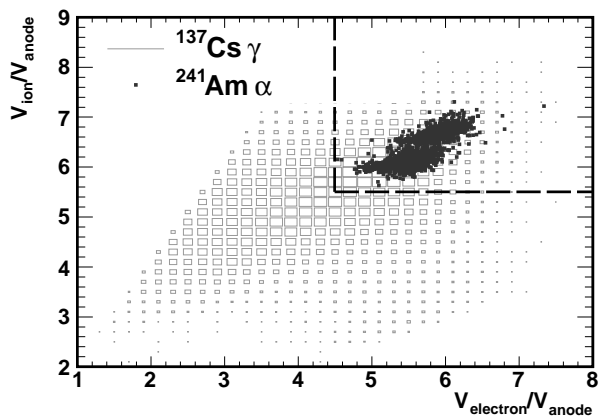


Figure 5: Ratio of mesh signal peaks to anode signal peak of electronic recoils and α tracks. The dashed line represents the selection cuts used to remove electrons.

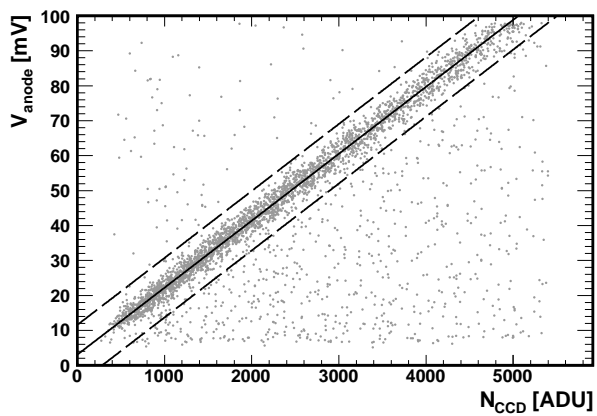


Figure 6: Energy of ^{241}Am track as measured by charge readout on the anode V_{anode} and by the CCD N_{CCD} . Solid line: best fit. Dashed lines: Energy matching cut limits, 3.5σ from best fit.

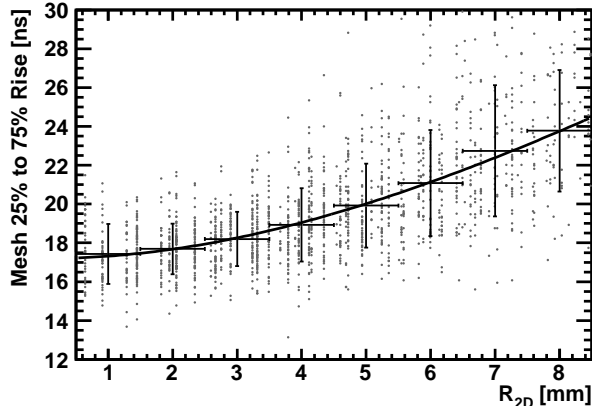


Figure 7: 25%-75% rise time vs. R_{2D} of low energy α tracks. The tracks are collimated with a mean angle of roughly 45° , so Δz increases with R_{2D} . The fit is to $T(R_{2D}) = \sqrt{T_0^2 + m^2 R_{2D}^2}$, where $T_0 = 17.19 \pm 0.06$ ns is the contribution to the rise time from diffusion and $m = 2.04 \pm 0.03$ ns/mm is the slope of the line at high R_{2D} . The error bars here represent the 1σ spread from the mean value. A large spread is expected due to both straggling effects and the initial energy and angle distribution of the source.

250 The α data was also used to evaluate the capability of using the rise time
 251 to measure the recoil Δz . Because the mean polar angle of the α particles is
 252 roughly 45° , the two-dimensional range (R_{2D}) measured by the CCD is roughly
 253 proportional to Δz . Due to straggling and imperfect collimation of the source,
 254 a range of α energies and incident angles is seen, so a wide range of Δz values
 255 is expected for a given R_{2D} . However, the mean value can still be used to
 256 determine a calibration between the rise time and R_{2D} . Fig. 7 shows the result
 257 using the 25% to 75% rise time of the mesh signal. The proportionality constant
 258 between this rise time variable and R_{2D} is measured to be 2.04 ± 0.03 ns/mm.

259 4. Background Rejection

260 4.1. Electronic recoils

261 To determine the ability of a DMTPC detector to reject electronic recoils,
 262 a collimated $5 \mu\text{Ci } ^{137}\text{Cs}$ source was placed above the cathode mesh, outside
 263 the fiducial volume of the detector. The monoenergetic 660 keV γ rays create
 264 a broad spectrum of electronic recoils across the entire energy range used for
 265 WIMP searches, while higher energy 512 keV and 1.2 MeV electrons from β
 266 decays may also be detected.

267 An average of 27 charge signals per 1 s exposure passed the noise and patho-
 268 logical event cuts during the ^{137}Cs data run. Pile-up in the charge signals is
 269 negligible at this event rate. However, the signals of all recoils are accumu-
 270 lated into a CCD image, so that a region where several recoils overlap may be

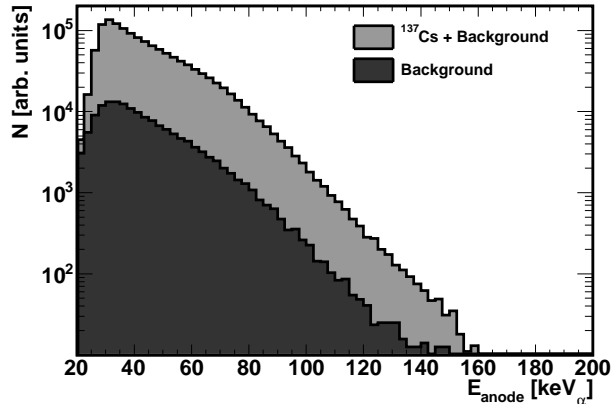


Figure 8: Light: Energy spectrum measured by the central anode channel in the ^{137}Cs run. Dark: Measured background spectrum scaled to match the live time of the ^{137}Cs run. The charge trigger efficiency decreases below 30 keV_α leading to the apparent peak in the spectrum.

271 misidentified as a nuclear recoil, even if any single recoil would not be observable
 272 above the CCD read noise.

273 A separate run with no sources inside the chamber was taken to measure
 274 the expected background spectrum. After removing events less than 3 seconds
 275 following a spark on the anode, a total of 51053 and 32568 one-second exposures
 276 were taken in the ^{137}Cs and background runs, respectively. The distribution of
 277 all charge events passing the initial set of noise and pathological-event cuts
 278 is used to determine the number of electronic recoils, as the trigger rate is
 279 dominated by electrons and minimum ionizing particles. The energy spectra
 280 of the two runs, after applying only the quality cuts identifying valid charge
 281 events, are shown in Figure 8.

282 In Monte Carlo studies, the CCD analysis used in this study has an efficiency
 283 of over 90% for nuclear recoils with energies between 40 keV_α and 200 keV_α . In
 284 this energy range, a total of 679919 charge events were measured in the ^{137}Cs
 285 run with an expected background of 77310 ± 350 . In the CCD analysis 20 tracks
 286 in the background run and 63 in the ^{137}Cs run pass all cuts without considering
 287 any charge cuts. The higher event rate in the ^{137}Cs run provides evidence
 288 for possible light pileup events; many CCD tracks occur near the track-finding
 289 energy threshold. The number of charge traces passing each set of cuts is given
 290 in Table 2.

291 The camera only images part of the amplification plane while the charge
 292 channels read out the entire plane. A background-subtracted sum of images
 293 taken during the ^{137}Cs run is used to estimate the fraction of electronic recoil
 294 events occurring within the region viewed by the CCD. A fit of this sum to a
 295 two-dimensional Gaussian distribution shows that roughly 68% of all ionization
 296 from electronic recoils occurs in this region. This value is known to within

	^{137}Cs	Background	Bkg.-Subtracted ^{137}Cs
Noise Cuts	679939	49339	602630±450
+Veto Cuts	38499	3891	32400±130
+ e^- Cuts	255	35	199±12
+Light Matching	5	3	-1.27 $^{+3.7}_{-3.3}$

Table 2: Number of charge triggers with $40 \text{ keV}_\alpha < E_{anode} < 200 \text{ keV}_\alpha$ that pass the specified cuts. The background subtraction includes the uncertainty of the background measurement.

roughly 15%. It is expected that approximately the same percentage of recoils also occur in the region read out by the CCD. Using this number and subtracting the expected background, 409770±430 electronic recoils occurred in the fiducial volume out of a total of 602600±350 with $40 \text{ keV}_\alpha < E < 200 \text{ keV}_\alpha$. Using these numbers, the CCD analysis alone achieves an electron rejection factor of 7.3×10^{-5} in this energy range. The charge analysis includes all recoils occurring in the field cage and rejects electron recoils at the level of 3.3×10^{-4} .

A combined analysis using both charge and CCD cuts as well as charge-light energy matching yields 5 events in the ^{137}Cs run and 3 events in the background run. Including the difference in total exposure time and the large uncertainties on both the background and combined background and signal distributions, a 90% confidence level upper limit on the electron recoil rejection factor of 1.1×10^{-5} is reached in the 40 keV_α to 200 keV_α energy range of the recoil spectrum of ^{137}Cs γ rays. From the detection efficiencies determined by Monte Carlo studies and the α source measurements, the detection efficiency for nuclear recoils using a combined CCD and charge analysis is determined to be over 63% for energies greater than 40 keV_α and over 80% for energies greater than 50 keV_α . A plot of the two-dimensional range as measured by the CCD against the recoil energy as measured by the anode channel shows (Fig. 9) that the passing events appear near the predicted three-dimensional range for nuclear recoils from SRIM. The two-dimensional range is shorter than the full three-dimensional range, so nuclear recoils are expected in a broad band with shorter ranges than the SRIM prediction. Furthermore, the peak pixel values for the tracks are well above the threshold used in track finding, indicating that the events are likely to be nuclear recoil or α backgrounds rather than signal pileup from electrons. If these events were excluded as likely nuclear recoils, the result would be statistics-limited at 5.6×10^{-6} .

4.2. CCD Backgrounds

Several classes of CCD background events appear in our detectors and have previously been eliminated through the use of CCD track selection cuts. While these cuts are generally able to identify and remove most such events, the charge readout analysis is also useful at eliminating these events. With the addition of the charge readout analysis, much less restrictive cuts can be used in the CCD analysis to maximize the efficiency for nuclear recoils. These background events include (1) residual bulk images, (2) intermittent hot pixels and (3) noise

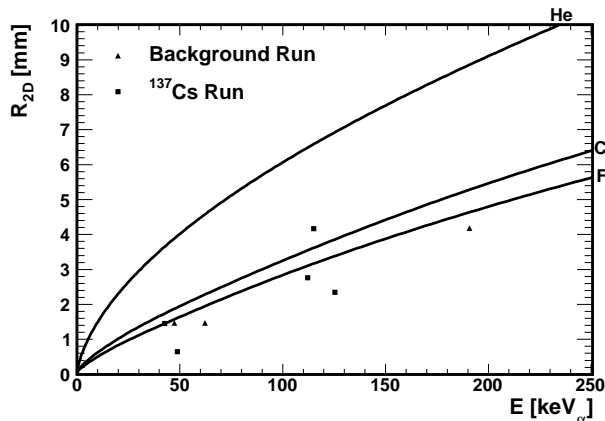


Figure 9: 2-dimensional range vs energy of events in the ^{137}Cs and background runs that pass all cuts. Solid lines are SRIM predictions for carbon, fluorine and helium tracks. The measured range is two-dimensional, while the SRIM curves give three-dimensional ranges so the measured points will generally fall below the SRIM prediction.

332 events. CCD backgrounds do not originate from ionization in the gas volume
 333 and so should have no associated charge signal.

334 Residual bulk images (RBI's) generally occur in our detectors when a spark
 335 inside the amplification region causes a great deal of light to hit the CCD. A
 336 fraction of the longer wavelength light penetrates deeply enough into the silicon
 337 to generate photoelectrons in the depletion region. With little to no electric
 338 field in this region, the free charge carriers must diffuse via thermal motion into
 339 the pixel potential wells. This can take several minutes [27]. The strength of the
 340 RBI signal is proportional to the exposure time and can sometimes mimic low
 341 energy nuclear recoils. Residual bulk images occur in front-illuminated CCDs
 342 such as the Kodak KAF-1001 chip used in the Apogee Alta U6 camera but not
 343 in back-illuminated CCDs.

344 Hot pixels and ionization from recoils occurring directly in the CCD chip are
 345 another source of background events found in the CCD event reconstruction.
 346 Hot pixels are a readout artifact where a single pixel is read out as containing
 347 an anomalously large amount of charge. Particles such as muons and γ rays
 348 incident on the CCD can also leave ionization inside the CCD silicon that will
 349 appear in one or more pixels. Such tracks typically leave much more charge per
 350 pixel than light from avalanches inside the detector gas volume.

351 While the cuts described in [17] are able to remove most of these CCD
 352 artifacts, they also can significantly reduce the reconstruction efficiency for low
 353 energy nuclear recoils, where nuclear recoils are more difficult to distinguish
 354 from the background noise of the CCD. Requiring coincidence between the light
 355 and charge signals provides additional rejection power of these types of events.
 356 The CCD analysis is less sensitive to recoils than the charge analysis due to the

Event type from CCD analysis	Before charge cuts	After charge cuts	Reduction [%]
RBI	1332	7	99.5 ± 0.2
Hot pixel/CCD Si Recoil	1246	11	99.1 ± 0.3
Edge Crossing (α)	17	0	100_{-9}^{+0}
Nuclear recoil/Out-of-time α	20	5	75 ± 11
All Tracks	2615	23	99.1 ± 0.2

Table 3: Number of CCD events of different types found before and after applying charge cuts, $25 \text{ keV}_\alpha < E_{CCD} < 400 \text{ keV}_\alpha$. The RBI and hot pixel/CCD Si recoil events are false coincidences between low energy charge signals and CCD artifacts with low apparent light signals.

357 favorable signal-to-noise ratio of the charge channels compared to the CCD.
358 In addition to these CCD artifacts another CCD-related background is “out-
359 of-time” events, which are recoils and α decays occurring during event readout.
360 When the CCD is being read out, charge is shifted from one pixel to another as
361 the charge from each pixel is digitized. A camera shutter is not used during data
362 acquisition so any scintillation occurring during the 0.2-0.3 s readout time will
363 appear shifted in the digitized image from its true position. The scintillation
364 light from an α particle depositing only a small fraction of its energy in the
365 imaged region can then be shifted toward the middle of the image, where it
366 might resemble a nuclear recoil. These events are very difficult to identify with
367 the CCD analysis. The charge channels do not collect data during this readout
368 time, so a coincident charge signal will not appear for these shifted events.

369 To evaluate the ability of the charge readout in removing these CCD back-
370 ground events in the energy range $25 \text{ keV}_\alpha < E_{CCD} < 400 \text{ keV}_\alpha$, a separate
371 analysis was performed on the data from the background run described in Sec.
372 4.1. A reduced set of CCD cuts identical to those used in Sec. 4.1 is used to
373 define different classes of CCD artifacts and to determine the fraction removed
374 by requiring charge-light coincidence. RBIs are defined as having at least two
375 CCD tracks occurring within 10 pixels (1.6 mm) of one another within a single
376 1000 event run. Hot pixels, ionization events in the CCD chip and noise events
377 are identified by three cuts. They 1) have a maximum pixel value greater than
378 500 ADU (38 keV), 2) include a pixel containing more than 30% of the total
379 light of the reconstructed track, or 3) do not include enough pixels far enough
380 above background to reconstruct a nonzero range. Tracks passing these cuts
381 but touching the edge of the image are typically α decays and are removed as
382 well. Any remaining tracks are tagged as nuclear recoil candidates or out-of-time
383 partial α events.

384 Requiring all CCD events to have a coincident charge signal removes more
385 than 99% of the RBI, noise, CCD Si track, and hot pixel events before applying
386 any of the CCD cuts. The few events of these types that did pass were due to
387 false coincidences between CCD and charge signals with very low energies. All
388 edge crossing events were removed, as would be expected since the CCD only

389 measures part of these events. Finally, $75 \pm 11\%$ of the events tagged as possible
390 nuclear recoils in the CCD-only analysis were also rejected, leaving 5 nuclear
391 recoil candidates having both charge and light signals. This indicates that many
392 of the events identified in the CCD analysis are likely either out-of-time nuclear
393 recoils and α decays or events from the other classes that were not identified by
394 the selection cuts (Table. 3).

395 5. Discussion and Conclusions

396 This work has demonstrated the ability to reject electronic recoils by a factor
397 of 1.1×10^{-5} at 90% C.L. level for electron recoils generated from a ^{137}Cs γ -
398 ray source with energies between 40 keV $_{\alpha}$ and 200 keV $_{\alpha}$ (or between 80 keV $_r$
399 and 300 keV $_r$ for fluorine recoils). Neither the charge nor the CCD analysis is
400 completely efficient at removing electrons when considered independently in this
401 analysis, but the combined result is significantly stronger. In an underground
402 WIMP search, the CCD analysis is expected to be much more effective due to
403 the greatly reduced recoil multiplicity per exposure compared to the ^{137}Cs run
404 shown here. Stronger selection cuts will also further enhance the ability of the
405 CCD analysis to reject electrons. The charge-light matching will also be much
406 more effective as the chance of finding a false coincidence will be greatly reduced
407 with the lower event rate in a source-free run.

408 It is also expected that the CCD and charge analyses are most sensitive
409 to different event topologies. The charge analysis is most effective at rejecting
410 electronic recoils with large Δz , while the CCD analysis is most efficient at
411 rejecting electrons with large projected two-dimensional range, perpendicular to
412 Δz . With a rejection power in this simple analysis of 7.3×10^{-5} in the CCD, $3.3 \times$
413 10^{-4} in charge, and additional rejection power gained by requiring charge-light
414 energy matching a rejection factor of order 10^{-8} could be achieved if the CCD
415 and charge analyses are in fact relatively uncorrelated. A much longer run would
416 be required to attempt to confirm such a hypothesis. Even with this rejection
417 power, the electron rejection analysis can be improved. Stronger cuts on recoils
418 found in the CCD have already been used by the DMTPC collaboration in
419 WIMP searches, although these also reduce the detector efficiency for signal
420 events. Further refinements in the charge reconstruction and selection cuts are
421 also expected in future analyses.

422 The addition of the charge signal analysis strengthens the ability of DMTPC
423 detectors to identify and remove CCD artifacts from the analysis by removing
424 more than 99% of such events before applying CCD-based nuclear recoil selec-
425 tion cuts. The charge analysis also allows for the identification and removal of
426 events occurring during CCD readout, which can mimic the signal of low-energy
427 nuclear recoils but cannot be easily identified with the CCD-only analyses used
428 previously by the DMTPC collaboration.

429 The ability to reject electronic recoils with high efficiency and without signifi-
430 cantly reducing the detection efficiency of nuclear recoils suggests that electronic
431 recoils are not expected to be a significant source of background events for the
432 target energy range of DMTPC detectors for WIMP searches.

433 **Acknowledgments**

434 The DMTPC collaboration would like to acknowledge support by the U.S.
435 Department of Energy (grant number DE-FG02-05ER41360), the Advanced De-
436 tector Research Program of the U.S. Department of Energy (contract number
437 6916448), as well as the Reed Award Program, the Ferry Fund, the Pappalardo
438 Fellowship program, the MIT Kavli Institute for Astrophysics and Space Re-
439 search, the MIT Bates Research and Engineering Center, and the Physics De-
440 partment at the Massachusetts Institute of Technology. We would like to thank
441 Mike Grossman for valuable technical assistance.

442 **References**

- 443 [1] C. E. Aalseth et al. Search for an Annual Modulation in a p -Type Point
444 Contact Germanium Dark Matter Detector. *Phys. Rev. Lett.*, 107:141301,
445 Sep 2011.
- 446 [2] G. Angloher et al. Results from 730 kg days of the CRESST-II Dark Matter
447 search. *Eur. Phys. J. C*, 72:1971, 2012.
- 448 [3] R. Bernabei et al. First results from DAMA/LIBRA and the combined
449 results with DAMA/NaI. *Eur. Phys. J. C*, 56:333–355, 2008.
- 450 [4] E. Aprile et al. Dark Matter Results from 100 Live Days of XENON100
451 Data. *Phys. Rev. Lett.*, 107:131302, Sep 2011.
- 452 [5] Z. Ahmed et al. Results from a Low-Energy Analysis of the CDMS II
453 Germanium Data. *Phys. Rev. Lett.*, 106:131302, Mar 2011.
- 454 [6] D.N. Spergel. Motion of the Earth and the detection of weakly interacting
455 massive particles. *Phys. Rev. D*, 37:1353–1355, 1988.
- 456 [7] J.D. Lewin and P.F. Smith. Review of mathematics, numerical factors,
457 and corrections for dark matter experiments based on elastic nuclear recoil.
458 *Astropart. Phys.*, 6:87–112, 1996.
- 459 [8] S. Ahlen et al. The case for a directional dark matter detector and the
460 status of current experimental efforts. *Int. J. Mod. Phys.*, A25:1–51, 2010.
- 461 [9] Anne M. Green and Ben Morgan. Optimizing WIMP directional detectors.
462 *Astropart. Phys.*, 27:142–149, 2007.
- 463 [10] Ben Morgan and Anne M. Green. Directional Statistics for WIMP direct
464 detection II: 2-d read-out. *Phys. Rev. D*, 72:123501, 2005.
- 465 [11] Ben Morgan, Anne M. Green, and Neil J. C. Spooner. Directional statistics
466 for WIMP direct detection. *Phys. Rev. D*, 71:103507, 2005.
- 467 [12] J. Billard, F. Mayet, and D. Santos. Exclusion limits from data of direc-
468 tional dark matter detectors. *Phys. Rev. D*, 82:055011, Sep 2010.

- 469 [13] J. Billard, F. Mayet, and D. Santos. Assessing the discovery potential of
470 directional detection of dark matter. *Phys. Rev. D*, 85:035006, Feb 2012.
- 471 [14] J. Billard, F. Mayet, and D. Santos. Markov chain monte carlo analysis to
472 constrain dark matter properties with directional detection. *Phys. Rev. D*,
473 83:075002, Apr 2011.
- 474 [15] S. Ellis and R. Flores. Elastic supersymmetric relic-nucleus scattering re-
475 visited. *Phys. Lett.*, B263:259–266, 1991.
- 476 [16] D. Dujmic et al. Charge amplification concepts for direction-sensitive dark
477 matter detectors. *Astropart. Phys.*, 30:58–64, 2008.
- 478 [17] S. Ahlen et al. First Dark Matter Search Results from a Surface Run of the
479 10-L DMTPC Directional Dark Matter Detector. *Phys. Lett.*, B695:124–
480 129, 2011.
- 481 [18] E. Behnke et al. Spin-dependent wimp limits from a bubble chamber.
482 *Science*, 319(5865):933–936, 2008.
- 483 [19] S. Archambault et al. Dark matter spin-dependent limits for WIMP inter-
484 actions on 19F by PICASSO. *Physics Letters B*, 682(2):185 – 192, 2009.
- 485 [20] S. Burgos et al. Studies of neutron detection and backgrounds with the
486 DRIFT-IIa dark matter detector. *Astroparticle Physics*, 28:409 – 421, 2007.
- 487 [21] D. Santos et al. MIMAC : A micro-tpc matrix for directional detection of
488 dark matter. *EAS Publications Series*, 53:25–31, 2012.
- 489 [22] H. Yegoryan. Study of Alpha Background in a Dark Matter De-
490 tector. *Senior Thesis, Massachusetts Institute of Technology*, 2010.
491 <http://dspace.mit.edu/handle/1721.1/61272>.
- 492 [23] J.F. Ziegler, J.P. Biersack, and M.D. Ziegler. SRIM: The Stopping and
493 Range of Ions in Matter. <http://www.srim.org/>, 2011.
- 494 [24] Cremat, 2012. <http://www.cremat.com>.
- 495 [25] Route2Electronics, 2012. <http://route2electronics.com>.
- 496 [26] L.G. Christophorou et al. Electron Interactions with CF₄. *J. Phys. Chem.*
497 *Re. Data.*, 25:1341–1388, 1996.
- 498 [27] James R. Janesick. *Scientific Charge-Coupled Devices*. SPIE, Bellingham,
499 WA, 2001.